### Title

Subtle Local Structural Details Influence Ion Transport in Glassy $Li^+$ Thiophosphate Solid Electrolytes




### Journal

ACS Applied Materials & Interfaces, 13(48)

### ISSN

1944-8244 1944-8252



### Authors

Preefer, Molleigh B
Grebenkemper, Jason H
Wilson, Catrina E
et al.



### Publication Date

2021-11-29

### DOI

10.1021/acsami.1c16515


### Data Availability

The data associated with this publication are in the supplemental files.


Peer reviewed

# Subtle Local Structural Details Influence Ion Transport in Glassy $Li^+$ Thiophosphate Solid Electrolytes

Molleigh B. Preefer,[*,†,‡] Jason H. Grebenkemper,[‡] Catrina E. Wilson,[†] Margaux Everingham,[†] Joya A. Cooley,[¶] and Ram Seshadri[*,‡,†]

†*Department of Chemistry and Biochemistry*

*University of California, Santa Barbara, California 93106, United States*

‡*Materials Department and Materials Research Laboratory*

*University of California, Santa Barbara, California 93106, United States*

¶*Department of Chemistry and Biochemistry*

*California State University, Fullerton, California 92834, United States*

E-mail: mpreefer@mrl.ucsb.edu; seshadri@mrl.ucsb.edu

**Abstract**

Many of the promising, high-performing solid electrolytes for lithium-ion batteries are amorphous or contain an amorphous component, particularly in the Li thiophosphate $Li_2S$–$P_2S_5$ compositional series (LPS). An explicit study of the local structure in four samples of ostensibly identically-prepared $70Li_2S$–$30P_2S_5$ glass reveals substantial variation in the ratio between the two main local structural units in this system: ${PS_4}^{3-}$ tetrahedra and ${P_2S_7}^{4-}$ corner-sharing tetrahedral pairs. Local structural and compositional probes including Raman spectroscopy, X-ray photoelectron spectroscopy, and X-ray pair distribution analysis are employed here to arrive at a consistent description of the relative amounts of isolated tetrahedral units, which vary by 13% across the samples measured. This local structure variation translates to differences in the activation energies measured by electrochemical impedance spectroscopy in these samples, such that the higher concentration of isolated tetrahedra corresponds to a lower activation energy. The measured temperature-dependent ionic conductivity data are compared to conductivity results across the literature reported on the same compositions, highlighting the variation in measured activation energy for nominally identical samples. These findings have implications for the critical need to play close attention to the local structure in solid electrolytes, particularly in systems that are glasses, glass-ceramics, or even comprise a small amorphous contribution.

## Keywords

solid electrolyte, lithium-ion conductor, lithium thiophosphate, amorphous, local structure

## Introduction

All-solid-state batteries are gaining momentum as a promising next-generation battery technology to obviate several concerns and limitations of current liquid-electrolyte–containing Li-ion cells.[1] Inorganic solid electrolytes are attractive because they have the potential to improve safety, simplify cell design, and potentially improve upon energy and power density.[2] However, there are many trade-offs to consider in order to identify materials that could be commercially viable.[3] There are many classes of inorganic solid electrolytes, including halides, oxides, and sulfides. One of the main trade-offs when comparing these three classes of materials is the electrochemical stability window versus Li and $Li^+$-ion conductivity at reasonable operating temperatures. Not surprisingly, the stability window and the conductivity are contraindicated, with (chemically) harder anion frameworks such as oxides and fluorides providing greater stability at the cost of the $Li^+$ being bound more strongly. Consequently, while fluorides offer some of the widest stability windows against Li, the $Li^+$-ion conductivity tends to be relatively poor.[4,5] Oxides can also have acceptable stability windows against Li, but conductivity is often still too low to yield practical replacements of liquid electrolytes.[4,5] Sulfides have been shown to exhibit $Li^+$-ion conductivity values on the same order as liquid electrolytes, but the stability window against Li is limited.[6–8] Clearly, several design considerations must be considered as workable solid electrolytes for all-solid-state batteries are developed.[9–11]

Sulfide materials exhibit some of the most promising $Li^+$-ion conductivity values, and have been widely studied as a consequence.[13] Within the lithium thiophosphate system $Li_2S$–$P_2S_5$, there are several stoichiometries and crystal structures explored in terms of preparative conditions, ionic conductivity, electrochemical stability versus Li, and mechan-

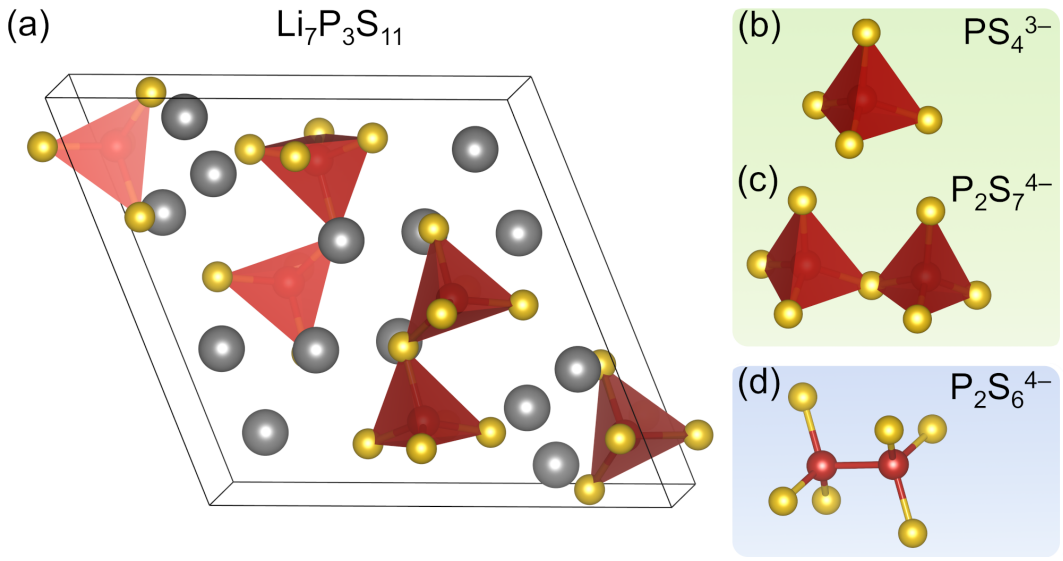


Figure 1: (a) Structure of $Li_7P_3S_{11}$, which crystallizes from the $70Li_2S$-$30P_2S_5$ glass in the $P\bar{1}$ space group (# 2). On the right, structural motifs observed in the $70Li_2S$-$30P_2S_5$ glass. (b) The isolated $PS_4^{3-}$ tetrahedron, *ie. ortho*-thiophosphate. (c) The corner-sharing $P_2S_7^{4-}$, *ie. pyro*-thiophosphate. (d) The $P_2S_6^{4-}$ dumbbell, *ie. hypo*-thiodiphosphate, which is a signature of the thermodynamically-stable $Li_4P_2S_6$ structure that can crystallize from the $70Li_2S$–$30P_2S_5$ glass. Structures were visualized using VESTA.[12]

ical properties, which are all parameters necessary to understand how these materials will perform in a cell. Especially within the $Li_2S$–$P_2S_5$ system, there are many stoichiometries that form glasses and glass-ceramics, which are crystalline domains stabilized within a glassy matrix. For $70Li_2S$–$30P_2S_5$, the glass-ceramic crystallizes into the $Li_7P_3S_{11}$ structure [figure 1(a)], and the glass is composed of two main structural motifs present in the $Li_7P_3S_{11}$ structure: isolated $PS_4^{3-}$ tetrahedra, *ie.*, the *ortho*-thiophosphate and corner-sharing $P_2S_7^{4-}$ tetrahedral pairs, *ie. pyro*-thiophosphate [figure 1(b,c)]. Since $Li_7P_3S_{11}$ is metastable, sometimes the less conductive, thermodynamically-stable product $Li_4P_2S_6$ will form simultaneously, so the $P_2S_6^{4-}$ dumbbell, *ie. hypo*-thiodiphosphate can also be present in the glassy structure [figure 1(d)]. While high crystalline $Li_7P_3S_{11}$ content leads to higher conductivity, the glass component is desirable for the compliant mechanical properties it can impart, which is important when considering constructing a full cell.[14–16]

Beyond pure lithium thiophosphates, there are also the $Li_4GeS_4$-$Li_3PS_4$ system (LGPS),[17–19] Si substitution in LGPS,[20,21] and argyrodites.[22–25] Even in systems that appear

crystalline, there can still exist some fraction that is glassy. For example, the LGPS-like compound $Li_7SiPS_8$ has a crystalline diffraction pattern, but through quantitative phase analysis using both Rietveld refinements on the x-ray diffraction patterns and integrating NMR spectra, Harm *et al* found between 5 wt.-% and 9 wt.-% of an amorphous contribution depending on the preparative conditions.[26] In many cases this glassy component would go undetected, but the local structure in these types of materials plays an important role. In order to fully understand the structure-property relationships in these materials, and therefore their function in all-solid-state cells, the entirety of the material must be carefully characterized. This becomes particularly critical when considering the myriad preparative routes being explored to prepare lithium thiophosphate phases,[27] which include solid-state,[28–30] mechanical ball-milling,[31–33] microwave-assisted,[34,35] and solution preparation,[11,36–38] as well as processing conditions used to densify the material for better performance in full cells.[14,39,40]

In this regard, it is also insightful to consider the recent, important inter-laboratory collaboration which highlighted different conductivity results from measuring the same argyrodite samples, synthesized and shared among the labs.[41] Room temperature conductivity values had a relative standard deviation of up to 50 %, and activation energies had a relative standard deviation of up to 15 %, indicating different densification procedures and measuring methods can yield different conductivity results.

Here we report on four effectively identically-prepared glassy samples of LPS, with the composition $70Li_2S–30P_2S_5$, prepared and measured using the same processing conditions and experimental setup. The samples were characterized comprehensively using a combination of high resolution synchrotron diffraction, Raman spectroscopy, X-ray photoelectron spectroscopy, X-ray pair distribution function analysis, and electrochemical impedance spectroscopy. We have been able to relate subtle changes in the local structure to differences in the activation energies and conductivities associated with $Li^+$-ion transport. The results obtained here are compared with a survey of those found in the literature to obtain

a comprehensive overview of this important class of $Li^+$-ion solid electrolytes.

# Methods

**Preparation of 70$Li_2S$–30$P_2S_5$ glass** The assisted-microwave preparation has been previously reported.[34] $Li_2S$ and $P_2S_5$ were ground until homogeneous in a 70:30 molar ratio using an agate mortar and pestle in an Ar filled glovebox with $H_2O$ and $O_2 < 0.1$ ppm. The powder was pressed into a 6 mm pellets weighing ≈250 mg each, and these were sealed in fused silica ampoules under 0.25 atm of Ar (3 inch long, 3/8 inch diameter). The ampoules were individually buried (1 per reaction) in the center of a 250 mL alumina crucible filled with 70g of activated charcoal (DARCO 12-20 mesh). The alumina crucible was then placed a cylinder of alumina fiberboard for insulation and placed off-center in a 1200 W microwave oven (Panasonic NN-SN651B). This was heated at power 4 (40 % of the total power) for 18 min followed by quenching the sample tube in water. This process was repeated for a total of 4 samples under identical conditions, including pellet size, mass, tube length, partial pressure, mass of charcoal, insulation, microwave conditions, and quenching. A previous procedure was followed for the melt-quench method which involves heating the $Li_2S$ and $P_2S_5$ mixture in a fused silica ampoule in a furnace at 70$Li_2S$–30$P_2S_5$ 700 °C and quenching in water in order to form an amorphous glass.[42]

**X-ray photoelectron spectroscopy** X-ray photoelectron spectroscopy (XPS) was carried out on a Kratos Axis Ultra X-ray Photoelectron Spectroscopy system with a monochromatic Al source K$\alpha$ (1.4 keV). Samples were prepared in an Ar-filled glovebox using a stainless steel sample stage with a cover that seals using an o-ring. Once transferred to the chamber, and the chamber was allowed to reach high vacuum, the cover was removed (inside of the chamber). Pass energies of 80 eV for high resolution scans were detected with a multi-channel detector. Dwell times were 80 ms and 5 scans were averaged. The spectra were fit by the least-squares method to pseudo-Voigt functions (Gaussian/Lorentzian 70/30) with

Shirley baselines using CasaXPS. All spectra were referenced to adventitious C $1s$ peak at 284.8 eV. The phosphorus $2p_{3/2}$ and $2p_{3/2}$ peaks were constrained to split by $\Delta = 0.87$ eV, with a relative area ratio of 2:1.

**Raman spectroscopy** Raman spectroscopic measurements were carried out under inert conditions using a Horiba LabRAM ARAMIS Raman spectrometer equipped with a confocal microscope. Samples were prepared in an Ar-filled glovebox by sealing a glass cover slip over the powder sample on a glass microscope slide. Data was collected with a 633 nm laser excitation, 500 $\mu$m hole, 500 $\mu$m slit, 1200 $\text{cm}^{-1}$ grating, 2 second exposures, and 5 spectra averaged, centered at 450 $\text{cm}^{-1}$. For the crystallization study, a 532 nm laser excitation was used instead. A TS1200 Linkam heating stage was employed to monitor spectra at different temperatures. Small glass crucibles were made to fit inside of the heating chamber, into which the powder was loaded in an Ar-filled glovebox. The top of the glass crucible was sealed with a 100 $\mu$m thick glass cover slip and high temperature epoxy (JB Weld). The laser was focused through the Linkam stage and the glass cover slip. Initial spectra were also acquired at 40 °C, 90 °C, and 190 °C to track the progression leading up to the crystallization temperature regime. Raman spectra were acquired from 240 °C to 310 °C in 5 °C intervals with 10 minute dwell times for equilibration. As a control, data was also collected on samples that were heated and exposed to air, and left in ambient conditions for several hours. This helped establish that the changes seen in the temperature-dependent Raman spectra did not arise due to sample degradation during the course of the crystallization experiments.

**Synchrotron X-ray scattering** High resolution synchrotron diffraction data was collected at room temperature at the Advanced Photon Source at Argonne National Laboratories, beamline 11-BM-B using an average wavelength of $\lambda = 0.414581$ Å. Samples were loaded into Kapton capillaries and sealed with epoxy inside of an Ar-filled glovebox. They were removed from inert atmosphere minutes prior to measurement. For the powder diffrac-

tion, approximately 10 wt.-% crystalline silicon was added to each sample (with known exact masses) in order to quantify any crystalline components observed in the material. However, since only amorphous scattering was observed, we did not perform any further refinements. Prior laboratory powder X-ray diffraction (XRD) data was collected using a Panalytical Empyrean diffractometer with Cu K$\alpha$ radiation (Supporting Information figure S.1). Powders were protected from the atmosphere utilizing an air sensitive holder containing a zero background plate and a Kapton film window. Total scattering data for pair distribution function (PDF, $G(r)$) analysis was acquired on powder samples in Kapton capillaries on beamline 11-ID-B at a wavelength of 0.2113 Å with a maximum momentum transfer $Q_{max}$ = 17.5 Å$^{-1}$. Frames of data were initially processed using GSAS-II[43] followed by converting the scattering using PDFGetX3.[44] Simulations were carried out using PDFgui.[45] The crystal structure of $Li_7P_3S_{11}$ ($P\bar{1}$, ICSD Entry 157654) was used, and the parameters employed were in the range of 0.1 Å to 30.0 Å with the scale factor = 1.0, $Q_{max}$ = 17.5 Å$^{-1}$, $Q_{damp}$ = 0.0347 Å$^{-1}$, and $Q_{broad}$ = 0.0103 Å$^{-1}$. The partials were calculated in a similar manner except prior to simulation in PDFgui, any elements other than the elements for the partial were removed from the structure. This edited structure was then used to simulate the corresponding partial PDF using the same parameters as before. $Q_{max}$ was determined from the experimental data as the highest achievable value that did not introduce Fourier transform artifacts. $Q_{damp}$ and $Q_{broad}$ were determined from real-space Rietveld refinement of a $CeO_2$ standard.

**Electrochemical impedance spectroscopy** Electrochemical impedance spectroscopy was measured using a VMP3 Bio-logic potentiostat from 1 MHz to 1 Hz with a 200 mV sinus amplitude under inert atmosphere. The samples were sintered under approximately 180 MPa pressure at 90 °C for 12 h before being subject to variable temperature measurements. Equilibrium was ensured for all of the data reported here by repeating measurements in succession at each temperature until each spectrum aligned before proceeding

with the next measurement. To ensure robust fits, data was collected from 20 °C to 90 °C in 5 °C increments using an environmental chamber. Spectra were also collected at 10 °C in order to clearly fit equivalent circuits to each sample, using ZFit in the ECLab software. Activation energies were calculated using an Arrhenius-type relationship with the Meyer-Neldel compensation, and uncertainties were propagated from uncertainties in the instruments used to acquire the data, namely the temperature chamber and the impedance analyzer. The custom cell design used has been described in detail in previous work.[34] A vise and a force gauge (Omega) were used to press pellets *in-situ* and apply and monitor pressure throughout the measurements.

**Comparison to prior literature results** Prior literature results were digitized from the plots presented in each corresponding reference. For the data not previously processed with the Meyer-Neldel compensation relation,[46] they were replotted so that the ordinate is $ln(\sigma T)$, and the activation energy was calculated from the resulting slopes. In the example of Busche *et al*, the calculated activation energy matched the reported activation using the Meyer-Neldel compensation, giving confidence to the digitization and processing.[39]

## Results and discussion

In order to understand how differences in local structure of identically-prepared samples correlate with their measured conductivity, first we set out to thoroughly characterize the structure of the materials. In order to confirm all of the glass samples are truly amorphous, high resolution synchrotron diffraction was used to characterize the long-range order in these materials [figure 2]. In case any crystalline component was found, the samples were preemptively spiked with 10 wt.% NIST standard Si, which would allow us to quantify the crystalline component, noticeably the sharp, high-intensity peaks in figure 2(a). However, no crystalline component relating to $Li_7P_3S_{11}$, $Li_4P_2S_6$, or any of the known crystalline phases in the Li–P–S ternary system were found and therefore the materials are all deemed

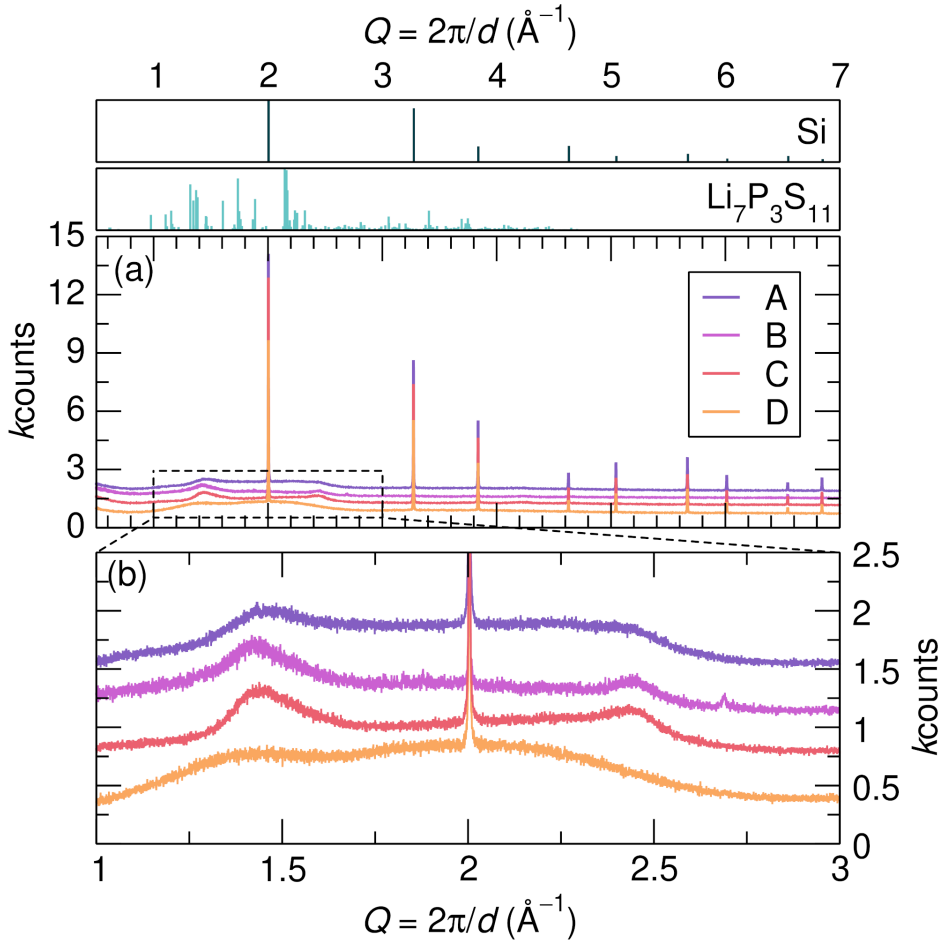


Figure 2: Synchrotron powder XRD of the 4 identically-prepared $70Li_2S$-$30P_2S_5$ glass samples. Silicon was added to the samples in order to quantify any amount of crystalline components identified in the diffraction pattern, though only amorphous contributions were detected. (a) The entire pattern from 1–7 $Å^{-1}$ shows the crystalline peaks from the added Si, which matches the expected reflections shown above. (b) A closer look at the highlighted region shows the complex amorphous background arising from the glassy samples.

to be amorphous. In one sample, a very small, unidentified impurity at 2.7 $\text{Å}^{-1}$ is noticeable, which may be an artifact from preparing the samples inside of the glovebox. It is interesting to note, however, that the amorphous background component in the different diffraction patterns, differ slightly [figure 2(b)]. The patterns for samples **B** and **C** are closely related, which is a theme throughout the characterization.

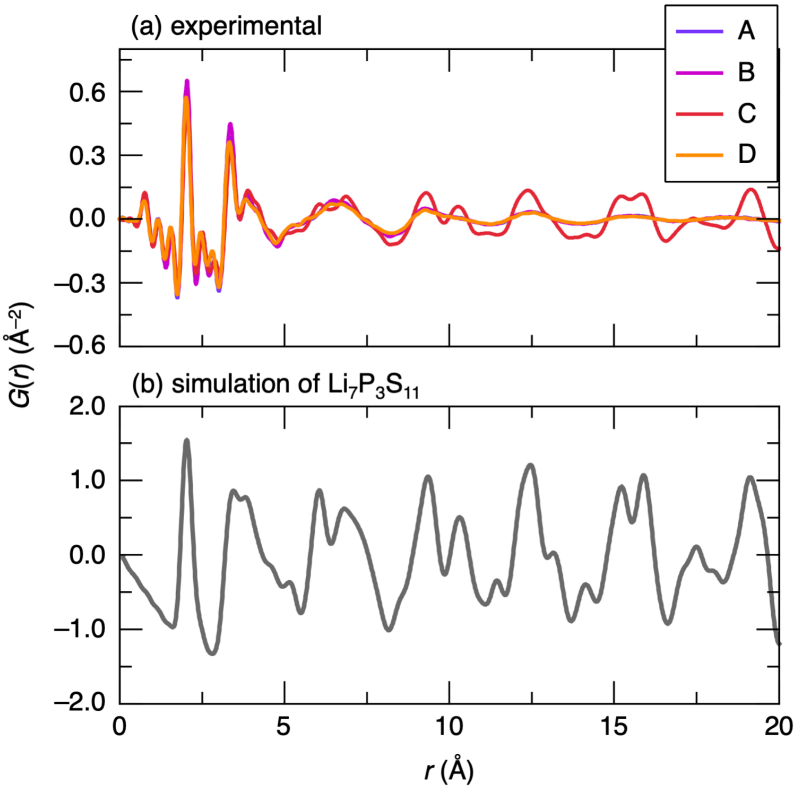


Figure 3: (a) Synchrotron X-ray pair distribution functions, $G(r)$ of the four compounds described here. (b) A simulation of the $G(r)$ of crystalline $Li_7P_3S_{11}$ for comparison.

Room-temperature synchrotron X-ray pair distribution functions, $G(r)$, of the four glass samples (data displayed in figure 3, compared with a simulation for crystalline $Li_7P_3S_{11}$, suggests that the local structure, particularly within about $r \approx 6$ Å, resembles the $G(r)$ of the crystalline phase that the glass can be transformed into though annealing. Interestingly, one of the samples, namely **C** displays correlations up to longer $r$ that resemble the crystalline phase. However, it should be noted that even in this sample, the relative intensity of these correlations is significantly subdued, suggesting perhaps a relatively mi-

nor amount of sample that is closer to possessing crystalline correlations on longer length scales. The complete description of the $G(r)$ of these amorphous compounds is beyond the scope of the current work, and would require extensive simulations of the structure using either empirical potentials or *ab-initio* methods.

Raman spectroscopy is a powerful tool to understand the structure in these materials. As a local structure probe, the modes corresponding to the two expected structural features in the glass can be identified. These modes are the strongest in the relevant spectral region, from 0 $cm^{-1}$ to 750 $cm^{-1}$ [figure 4(a)]. Overall, the spectra between the 4 samples are markedly reproducible, exhibiting all of the same peaks at the same positions. A closer look at the region between 340 $cm^{-1}$ and 475 $cm^{-1}$ shows the fine details in intensity in these modes [figure 4(b)]. From previous literature, the mode at 410 $cm^{-1}$ can be assigned to the corner-sharing tetrahedra, and the mode at 423 $cm^{-1}$ can be assigned to the isolated tetrahedron.[28,47] The spectra were normalized to the intensity of the corner-sharing tetrahedra in order to clearly see how the ratios of the corner-sharing tetrahedra and the isolated tetrahedra differ across the 4 samples. Sample **A** has the highest amount of the isolated tetrahedra. Samples **B** and **C** have very similar ratios, though **B** is slightly higher in the isolated tetrahedra. Finally, sample **D** has much less of the isolated tetrahedra, signaled by the clear decrease in the mode at 423 $cm^{-1}$. These are relatively large differences in intensity when compared directly that might otherwise go unnoticed. It is also pertinent to note that this is not simply an artifact of the assisted-microwave preparation conditions. We observe similar effects in samples prepared consistently with the melt quench method in an internal study (Supporting Information figure S.2). Since the intensity of the modes differ based on selection rules, these local structure observations remain qualitative. However, XPS provides a quantitative route to characterizing the amount of each structural unit across the four samples.

The phosphorus 2p binding energy region is especially telling of the quantitative ratio of the isolated and corner-sharing tetrahedra. A single, convoluted peak-shape is observed for

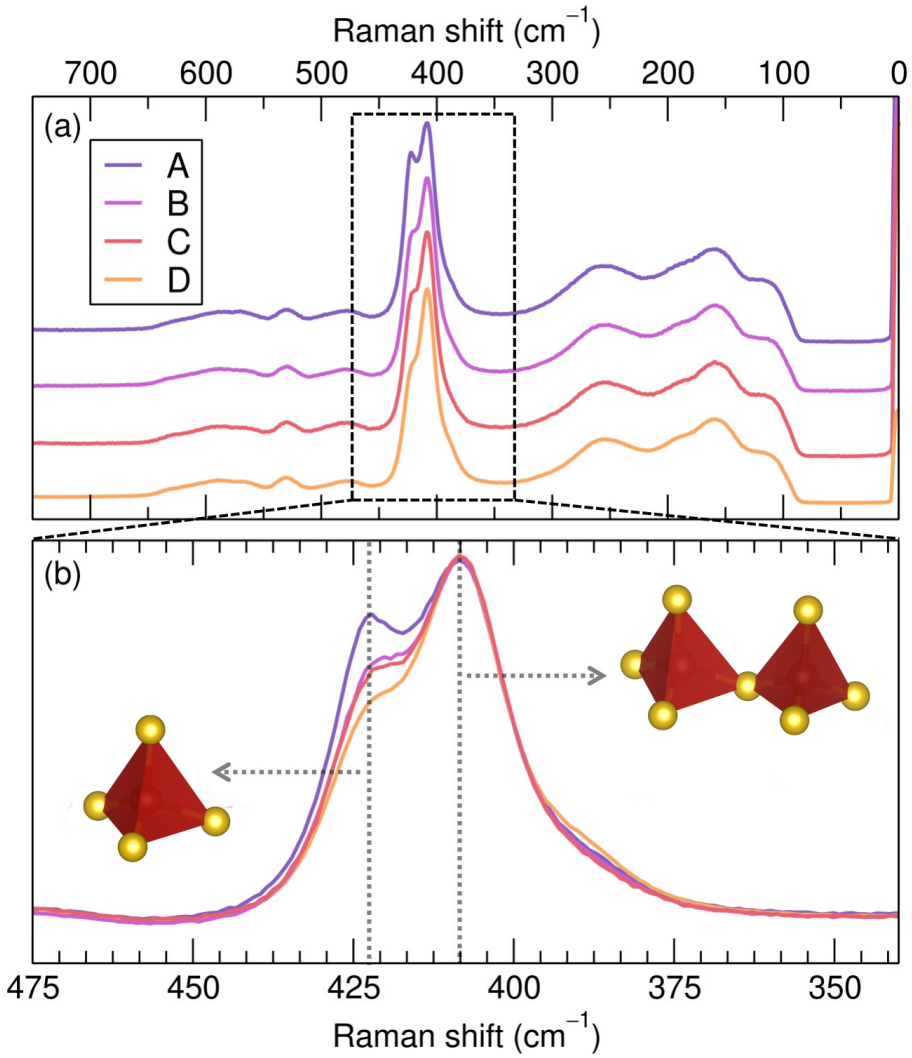


Figure 4: Raman spectroscopy is extremely sensitive to the local structure differences of the 4 identically-prepared $70Li_2S$–$30P_2S_5$ glass samples. The spectra were all normalized to the highest intensity peak and strongest mode at 408 cm$^{-1}$. (a) The entire spectrum shows the same peaks exist for each sample, confirming they are structurally alike. (b) The peaks characteristic of the corner-sharing tetrahedra (408 cm$^{-1}$) and isolated tetrahedra (423 cm$^{-1}$) highlight the subtle local structure differences, in which the ratio of these structural features can vary significantly.

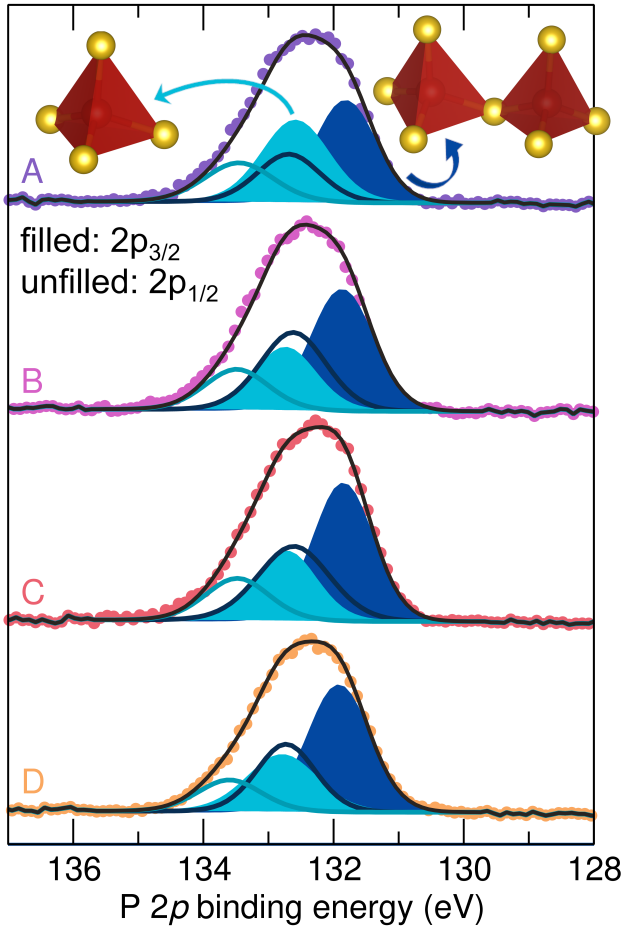


Figure 5: P 2p binding energy region from high resolution X-ray photoelectron spectroscopy of all 4 $70Li_2S$–$30P_2S_5$ glass samples. The lower binding energy $2p_{3/2}$ peak corresponds to the P in the corner-sharing tetrahedra environment (shaded dark blue), and the higher binding energy $2p_{3/2}$ peak corresponds to the P in the isolated tetrahedron (shaded light blue). The corresponding $2p_{1/2}$ peaks for both environments, shifted toward higher binding energies by $\Delta = 0.87$ eV, are not shaded (outlines only). Quantitative analysis was only performed using the results from the $2p_{3/2}$ peaks. The samples follow a consistent trend as seen in the Raman spectroscopy results.

all 4 samples, consistent with previous reports for $70Li_2S–30P_2S_5$ glasses.[34,39] The broad peak between 130 eV and 135 eV can be deconvoluted into 4 distinct peaks, which in turn correspond to 2 distinct P states due to the closely-spaced spin-orbit components (P $2p_{3/2}$ and P $2p_{1/2}$) [figure 5]. The lower binding energy peak (132 eV) is assigned to the P environment within the corner-sharing tetrahedra ($P_2S_7^{4-}$) while the higher binding energy peak (132.7 eV) is assigned to the P environment within the isolated tetrahedron ($PS_4^{3-}$), extensively characterized in previous studies.[7,39] For clarity, it's easiest to compare the P $2p_{3/2}$ peaks against each other across samples (signified by the shaded peak fits in 5). Qualitatively, the spectra all appear to be similar, with less of the state corresponding to the isolated tetrahedra than the corner-sharing tetrahedra, as expected according to the composition of the material. The higher binding energy peak appears to decrease from sample **A** through sample **D**.

Table 1: Quantitative fitting of the P $2p_{3/2}$ peaks across all 4 samples.

| | | $2p_{3/2}$ position (eV) | FWHM | area | % area | S:P ratio |
|---|---|---|---|---|---|---|
| **A** | corner-share<br>isolated | 131.9<br>132.8 | 1.08<br>1.20 | 1130.2<br>1002.9 | 53.0%<br>47.0% | 3.74:1 |
| **B** | corner-share<br>isolated | 132.0<br>132.8 | 1.11<br>1.19 | 1386.5<br>956.5 | 59.2%<br>40.8% | 3.71:1 |
| **C** | corner-share<br>isolated | 131.9<br>132.6 | 1.07<br>1.29 | 1507.0<br>991.8 | 60.3%<br>39.7% | 3.70:1 |
| **D** | corner-share<br>isolated | 131.9<br>132.6 | 1.11<br>1.06 | 1443.3<br>741.1 | 66.1%<br>33.9% | 3.67:1 |

This can be described quantitatively by comparing the values corresponding to the peak areas, as reported in Table 1. These quantification results are consistent with the trends observed in the Raman spectroscopy, such that sample **A** has the highest concentration of the isolated tetrahedra, followed by samples **B** and **C** (which are very similar), and sample **D** has the lowest concentration of the isolated tetrahedra. The greatest difference, between sample **A** and **D**, is a 13% decrease in concentration of isolated tetrahedra in **D**. Additionally, the similarity between **B** and **C** observed in the XRD and Raman spectroscopy

is persists in the XPS quantification. **B** has a slightly higher concentration of the isolated tetrahedra than **C** by 1.1%. The overall S:P ratio per sample can then be calculated based on the relative amounts of the two structural motifs. For the $70Li_2S$–$30P_2S_5$ composition, the ideal S:P ratio is 3.67:1. While all of the samples are within a reasonable range, all of the samples besides **D** are slightly enriched in sulfur. This suggest that the "ideal" composition of the glass should contain approximately 66% corner-sharing tetrahedra and 34% isolated tetrahedra.

While we have established that there is a clear trend in the differences in the local structure between the identically-prepared samples, it is also important to understand how this affects the conductivity in this material. Electrochemical impedance spectroscopy was used to characterize the intrinsic Li conductivity in all of the samples (blocking electrode setup). Spectra were collected from 20 °C to 85 °C in 5 degree increments to also calculate the activation energy associated with the Li conductivity [figure 6(a)]. Each spectra were fit to a modified Debye circuit in order to extract the bulk resistance [figure 6(b)], which then was converted to conductivity values using the geometry of the densified sample.

The activation energies for the 4 glass samples were calculated using an Arrhenius-type relationship with the Meyer-Neldel compensation:[46,48]

$$\sigma T = \sigma_0 \exp\left(\frac{-E_A}{k_B T}\right) \tag{1}$$

where $\sigma_0$ is the pre-factor, $E_A$ is the activation energy, and $k_B$ is the Boltzmann constant. The Meyer-Neldel compensation was used to take thermally-activated hopping into account (incorporated into the pre-factor term) for an intrinsic Li-ion conductor.[49]

The activation energies are particularly illustrative of how the variations described in the local structure are significant to the properties and function of the material [figure 6(c)]. Sample **A** has the lowest activation energy of $364 \pm 4$ meV, and **D** has the highest activation energy of $405 \pm 5$ meV, suggesting a higher concentration of the isolated tetrahedra facilitates Li migration in LPS glasses. **B** also has a lower activation energy than

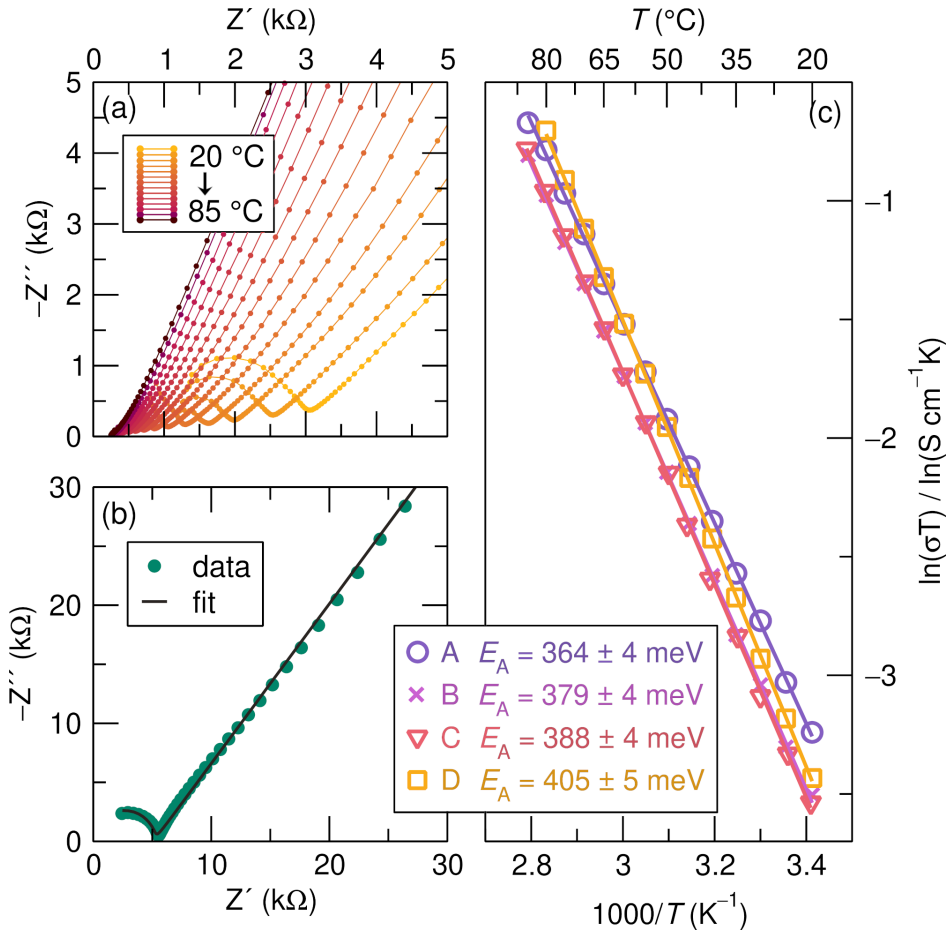


Figure 6: Electrochemical impedance spectroscopy in a blocking electrode (stainless steel) setup of the $70Li_2S–30P_2S_5$ glass. (a) Representative series of spectra from one of the glass samples showing the evolution of the spectra as a function of temperature, from 20 °C to 85 °C. (b) A representative spectrum at 10 °C with the equivalent circuit fit overlaid. (c) The conductivity of the 4 glass samples as a function of temperature fit to an Arrhenius-type relationship with a Meyer-Neldel correction. The corresponding activation energies for each sample is listed in the legend in units of meV.

**C** by 9 meV, the least difference between any other sample pair. This corresponds to **B** containing slightly more isolated tetrahedra than **C**, which has been consistent throughout all of the characterization described. The room temperature conductivities (298 K) of all of the samples are on the order of $10^{-4}$ S cm$^{-1}$. There are also slight variations between these values, with **A** having the highest room temperature conductivity. Interestingly, **D**'s conductivity is slightly higher than **B** and **C**. Since a single conductivity value is highly dependent on measurement conditions, the activation energies reported are much more indicative of the trends within the materials.

Table 2: Summary of the activation energies and room temperature conductivities found in each corresponding study, along with the preparation method for the $70Li_2S$–$30P_2S_5$ glasses.

| | preparation method | $E_A$ (meV) | $\sigma$ (S cm$^{-1}$) at 298 K |
|---|---|---|---|
| Busche *et al*[39] | mechanochemical | 425 | $1.86 \times 10^{-4}$ |
| Wenzel *et al*[7] | mechanochemical | 373 | $3.83 \times 10^{-5}$ |
| Dietrich *et al*[50] | mechanochemical | 448 | $3.58 \times 10^{-5}$ |
| Hayashi *et al*[31] | mechanochemical | 433 | |
| Mizuno *et al*[47] | melt quench | 415 | $5.00 \times 10^{-5}$ |
| Minami *et al*[51] | melt quench | 365 | |
| Minami *et al*[29] | melt quench | 360 | |
| Seino *et al*[6] | melt quench | 389 | $5.00 \times 10^{-5}$ |
| **A** (this work) | assisted-MW | 364 | $1.63 \times 10^{-4}$ |
| **B** (this work) | assisted-MW | 379 | $1.23 \times 10^{-4}$ |
| **C** (this work) | assisted-MW | 388 | $1.20 \times 10^{-4}$ |
| **D** (this work) | assisted-MW | 405 | $1.39 \times 10^{-4}$ |
| | | | |
| standard dev | | 28.2 | $5.46 \times 10^{-5}$ |
| average | | 395 | $1.01 \times 10^{-4}$ |

To put these values in context with previous results on this well-studied material, there is a considerable spread of reported values for reported $70Li_2S$–$30P_2S_5$ glasses [figure 7]. The conductivity data presented in this study is plotted concurrently with data mined from 8 other studies, specifically of the glass in this exact chemical composition. Since the data is reported inconsistently, where in some cases the Meyer-Neldel compensation is applied and in others a simple Arrhenius relationship is applied, the data was replotted to include

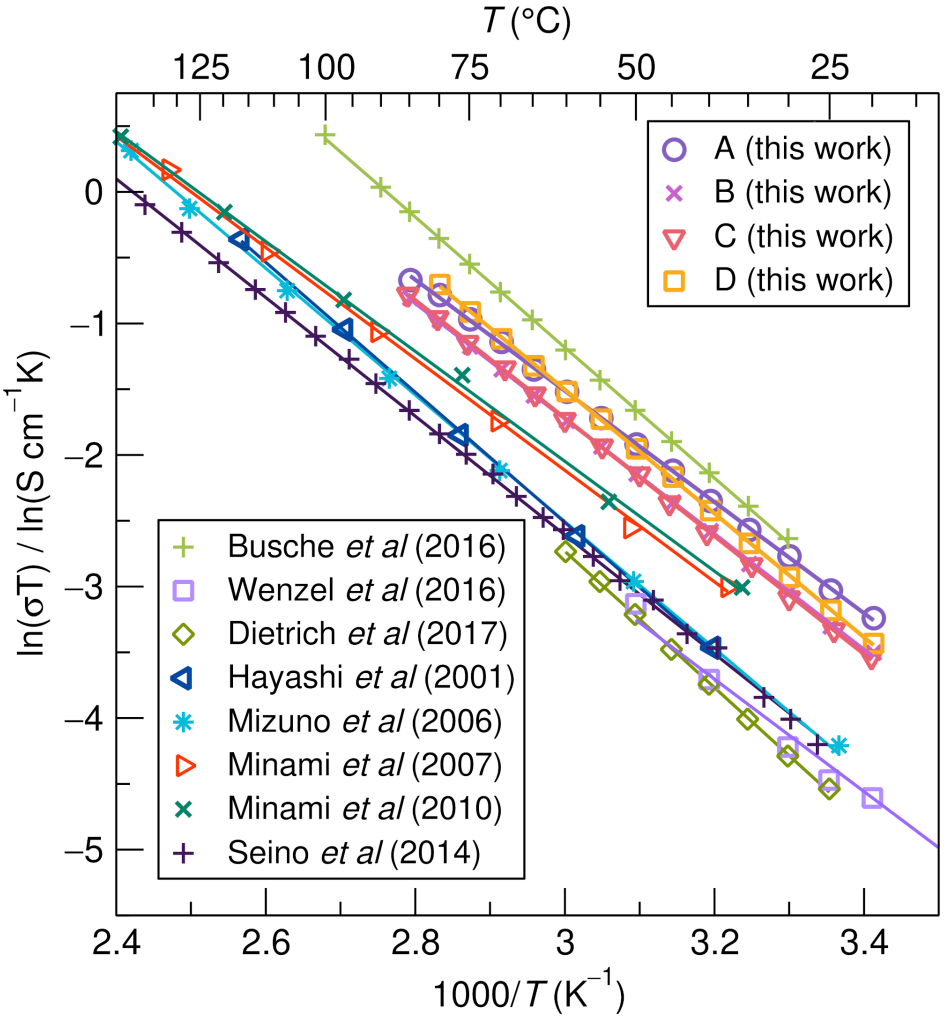


Figure 7: Arrhenius-type analysis with Meyer-Neldel compensation of the 4 glass samples presented in this work overlaid with similar samples from prior literature. All of the data corresponds to glass $70Li_2S–30P_2S_5$ samples, as described in each work, showing a distribution of results within the same glass Li thiophosphate system. The data was digitized and, when necessary, replotted with the Meyer-Neldel compensation such that all of the datasets are treated identically. Each dataset is fit to a linear equation, and the slope of that equation was used to calculate activation energies. The activation energies calculated and room temperature conductivity values are reported in a subsequent table. Some data was truncated for clarity of comparisons.

the Meyer-Neldel compensation if not already in that form. It is immediately apparent that there are both differences in the activation energies (indicated by the slopes of the Arrhenius relationships) and the room temperature conductivity values.

Table 2 lists the activation energy values in meV, the room temperature conductivity, and the preparation method for each glass sample. The comparison is based on the assumption that the samples prepared are truly glass samples, and not glass-ceramic samples that are partially crystalline. Given the room temperature conductivity values, we believe this is a valid assumption. One important caveat to keep in mind while comparing these samples is that conductivity measurement conditions lab-to-lab can differ, which may also affect the spread in reported values.[41] However, the local structure variation that likely exists is also convoluted with the differing measurement conditions. This leads to an overall standard deviation of 28.2 meV for the activation energy of the $70Li_2S$–$30P_2S_5$ glass, and the average activation energy is 395 meV.

Since more attention for practical applications is given to the superionic conductor glass-ceramic ($Li_7P_3S_{11}$) due to its higher conductivity, it is of interest to elucidate how these local structure effects propagate throughout the crystallization process. While there have been other studies previously on the crystallization process, specific emphasis here is placed on what happens to the ratio of the isolated and corner-sharing tetrahedra during annealing. Previous results from differential scanning calorimetry and other crystallization experiments suggest the crystallization process begins around 240 °C, and many glass-ceramic samples are prepared by annealing the glass between 260 °C and 280 °C for 1 or 2 hours before a significant amount of the undesirable (and thermodynamically-stable) $Li_4P_2S_6$ forms.[52] Therefore, a few spectra prior to the accepted crystallization regime were recorded at 40 °C, 90 °C, and 190 °C [figure 8(b)]. Data over a wider spectral range is displayed in the Supporting Information (figure S.3). At these temperature points the spectra are reproducible, with the same ratios of the isolated and corner-sharing tetrahedra. When the sample reaches the crystallization regime, there is a noticeable shift in

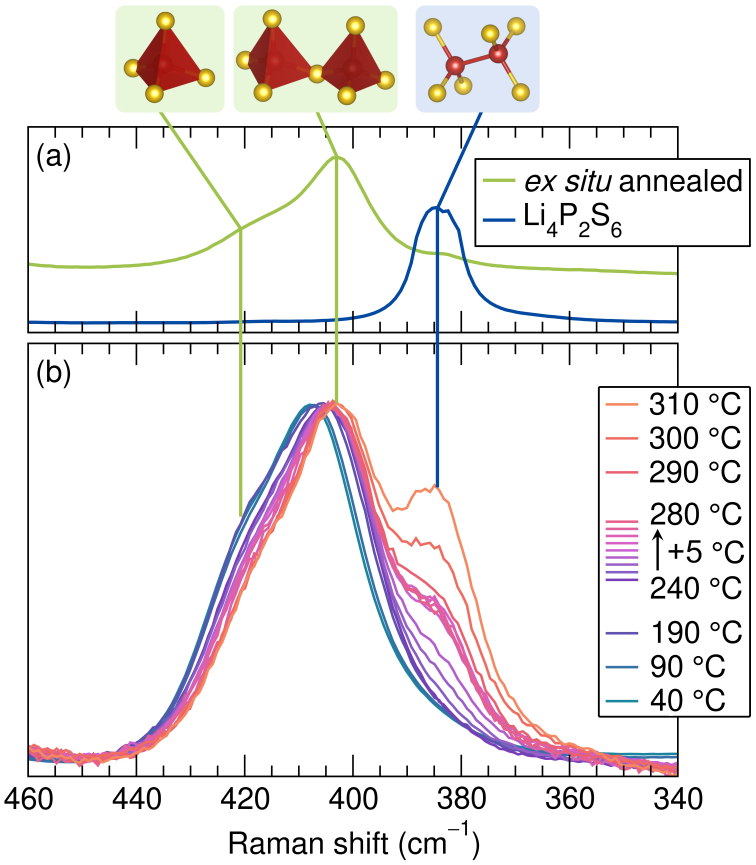


Figure 8: Raman spectroscopy of a representative glass (sample **D**) as it is heated *in situ* from 40 °C to 310 °C, causing it to crystallize. (a) Standards to understand the evolution of the spectrum as the sample is annealed. The significant structural features are depicted above, corresponding to the labeled peaks. (b) Spectra normalized to the corner-sharing tetrahedra peak at 410 $cm^{-1}$ (average). Data was collected more densely between 240 °C and 280 °C, in the region that has previously been recorded to induce crystallization. The sample and laser were not adjusted during the annealing process, so signal-to-noise decreases steadily throughout, likely due to the transformations of the material. The significant changes observed are: a decrease in the peak intensity associated with the isolated tetrahedron (421 $cm^{-1}$), a shift in the peak associated with the corner-sharing tetrahedra toward lower wavenumbers (403 $cm^{-1}$), and an increase in the peak intensity associated with the $P_2S_6^{4-}$ dumbbell (385 $cm^{-1}$), a signature of the $Li_4P_2S_6$ structure.

the peak positions toward lower wavenumbers, which is consistent with previous literature. Simultaneously, the intensity of the peak associated with the isolated tetrahedra begins to decrease (in this view where the peaks are normalized to the peak associated with the corner-sharing tetrahedra). This is notably before any discernible amount of the $Li_4P_2S_6$ phase begins to form, so inducing crystallization naturally decreases the ratio of the isolated:corner-sharing tetrahedra. After 255 °C, a detectable amount of the $Li_4P_2S_6$ phase grows, and by 265 °C through 280 °C, the peak associated to the $P_2S_6^{4-}$ dumbbell remains a consistent intensity, along with the peak associated with the isolated tetrahedra. Above 280 °C, the $Li_4P_2S_6$ phase increases significantly. A control experiment was conducted for which a sample was heated and exposed to air in order to make sure the assignments were indicative of the local structure changing due to crystallization and not due to air exposure (Supporting Information figures S.3 and S.4). The spectra collected for the crystallization study are indicative of a mixture of structural units comprising $Li_7P_3S_{11}$ and $Li_4P_2S_6$, and no evidence of air exposure was found. The *in-situ* measurements through the crystallization temperature were performed on sample **D**, but the trends are expected to be consistent regardless of the initial ratio of the structural motifs.

While many studies have highlighted the importance of processing conditions for tuning conductivity values in glass-ceramic solid electrolytes, *ie* hot-pressing versus cold pressing, or different preparation conditions leading to different ratios of crystalline versus amorphous components, another factor to be cognizant of is sample-to-sample variation. The glassy nature of these materials lends itself to differences in the local structure, which in turn affect the conductivity properties.

# Conclusion

The local structures of identically-prepared $70Li_2S$–$30P_2S_5$ glass samples were studied through Raman spectroscopy and XPS, showing variation in the ratio of isolated to corner-

sharing tetrahedra across the different samples. This translates to the activation energies calculated from EIS measurements, delineating that samples with higher amounts of the isolated tetrahedra have lower activation energies. This ratio of isolated to corner-sharing tetrahedra changes throughout the crystallization process, when the glass is heated through 280 °C. Especially when keeping in mind practical applications, this study highlights the need for in-depth understanding of the local structure in these materials, since they will affect the performance of all-solid-state batteries.

## Supporting Information Available

Laboratory XRD on the 4 glass samples, Raman characterization comparison of samples made through the traditional melt-quench method compared with the microwave-prepared samples described in this work, and expanded spectral-range data for the *in situ* Raman crystallization experiments.

## Acknowledgement

This work was supported by BASF Corporation through the California Research Alliance. The research reported here made use of shared facilities of the UC Santa Barbara Materials Research Science and Engineering Center (MRSEC, NSF DMR 1720256), a member of the Materials Research Facilities Network (www.mrfn.org). Diffraction data was collected at the X-ray Science Division beamline 11-BM and total scattering data was collected at 11-ID-B at the Advanced Photon Source, Argonne National Laboratory, a U.S. Department of Energy (DOE) Office of Science User Facility operated for the DOE Office of Science by Argonne National Laboratory under Contract No. DE-AC02-06CH11357. We gratefully acknowledge Professor David Clarke (Harvard University) for use of the Raman spectrometer and Linkam stage used for the crystallization study, and Principal Beamline Specialist

Kevin Beyer at beamline 11-ID-B for help with synchrotron X-ray data collection.

# References


(1) Janek, J.; Zeier, W. G. A Solid Future for Battery Development. *Nat. Energy* **2016**, *1*, 16141.

(2) Manthiram, A.; Yu, X.; Wang, S. Lithium Battery Chemistries Enabled by Solid-State Electrolytes. *Nat. Rev. Mater.* **2017**, *2*, 16103.

(3) Famprikis, T.; Canepa, P.; Dawson, J. A.; Islam, M. S.; Masquelier, C. Fundamentals of Inorganic Solid-State Electrolytes for Batteries. *Nat. Mater.* **2019**, *18*, 1278–1291.

(4) Zhu, Y.; He, X.; Mo, Y. Origin of Outstanding Stability in the Lithium Solid Electrolyte Materials: Insights from Thermodynamic Analyses Based on First-Principles Calculations. *ACS Appl. Mater. Interfaces* **2015**, *7*, 23685–23693.

(5) Richards, W. D.; Miara, L. J.; Wang, Y.; Kim, J. C.; Ceder, G. Interface Stability in Solid-State Batteries. *Chem. Mater.* **2016**, *28*, 266–273.

(6) Seino, Y.; Ota, T.; Takada, K.; Hayashi, A.; Tatsumisago, M. A Sulphide Lithium Super Ion Conductor is Superior to Liquid Ion Conductors for Use in Rechargeable Batteries. *Energy Environ. Sci.* **2014**, *7*, 627–631.

(7) Wenzel, S.; Weber, D. A.; Leichtweiss, T.; Busche, M. R.; Sann, J.; Janek, J. Interphase Formation and Degradation of Charge Transfer Kinetics between a Lithium Metal Anode and Highly Crystalline $Li_7P_3S_{11}$ Solid Electrolyte. *Solid State Ionics* **2016**, *286*, 24–33.

(8) Zhang, Q.; Cao, D.; Ma, Y.; Natan, A.; Aurora, P.; Zhu, H. Sulfide-Based Solid-State Electrolytes: Synthesis, Stability, and Potential for All-Solid-State Batteries. *Adv. Mater.* **2019**, *31*, 1–42.

(9) Wang, Y.; Richards, W. D.; Ong, S. P.; Miara, L. J.; Kim, J. C.; Mo, Y.; Ceder, G.

Design Principles for Solid-State Lithium Superionic Conductors. *Nat. Mater.* **2015**, *14*, 1–23.

(10) Lotsch, B. V.; Maier, J. Relevance of Solid Electrolytes for Lithium-Based Batteries: A Realistic View. *J. Electroceramics* **2017**, *38*, 128–141.

(11) Park, K. H.; Bai, Q.; Kim, D. H.; Oh, D. Y.; Zhu, Y.; Mo, Y.; Jung, Y. S. Design Strategies, Practical Considerations, and New Solution Processes of Sulfide Solid Electrolytes for All-Solid-State Batteries. *Adv. Energy Mater.* **2018**, *8*, 1–24.

(12) Momma, K.; Izumi, F. VESTA 3 for Three-Dimensional Visualization of Crystal, Volumetric and Morphology Data. *J. Appl. Crystallogr.* **2011**, *44*, 1272–1276.

(13) Lau, J.; DeBlock, R. H.; Butts, D. M.; Ashby, D. S.; Choi, C. S.; Dunn, B. S. Sulfide Solid Electrolytes for Lithium Battery Applications. *Adv. Energy Mater.* **2018**, *8*, 1800933.

(14) Sakuda, A.; Hayashi, A.; Tatsumisago, M. Sulfide Solid Electrolyte with Favorable Mechanical Property for All-Solid-State Lithium Battery. *Sci. Rep.* **2013**, *3*, 2–6.

(15) Kato, A.; Yamamoto, M.; Sakuda, A.; Hayashi, A.; Tatsumisago, M. Mechanical Properties of $Li_2S$-$P_2S_5$ Glasses with Lithium Halides and Application in All-Solid-State Batteries. *ACS Appl. Energy Mater.* **2018**, *1*, 1002–1007.

(16) McGrogan, F. P.; Swamy, T.; Bishop, S. R.; Eggleton, E.; Porz, L.; Chen, X.; Chiang, Y. M.; Van Vliet, K. J. Compliant Yet Brittle Mechanical Behavior of $Li_2S$-$P_2S_5$ Lithium-Ion-Conducting Solid Electrolyte. *Adv. Energy Mater.* **2017**, *7*, 1–5.

(17) Kuhn, A.; Duppel, V.; Lotsch, B. V. Tetragonal $Li_{10}GeP_2S_{12}$ and $Li_7GePS_8$ – Exploring the Li Ion Dynamics in LGPS Li Electrolytes. *Energy Environ. Sci.* **2013**, *6*, 3548–3552.

(18) Weber, D. A.; Senyshyn, A.; Weldert, K. S.; Wenzel, S.; Zhang, W.; Kaiser, R.; Bere,;

Ndts, S.; Janek, J.; Zeier, W. G. Structural Insights and 3D Diffusion Pathways within the Lithium Superionic Conductor $Li_{10}GeP_2S_{12}$. *Chem. Mater.* **2016**, *28*, 5905–5915.

(19) Tsukasaki, H.; Mori, S.; Shiotani, S.; Yamamura, H.; Iba, H. Direct Observation of a Non-Isothermal Crystallization Process in Precursor $Li_{10}GeP_2S_{12}$ Glass Electrolyte. *J. Power Sources* **2017**, *369*, 57–64.

(20) Ong, S. P.; Mo, Y.; Richards, W. D.; Miara, L.; Lee, H. S.; Ceder, G. Phase Stability, Electrochemical Stability and Ionic Conductivity of the $Li_{10}MP_2X_{12}$ (M = Ge, Si, Sn, Al or P, and X = O, S or Se) Family of Superionic Conductors. *Energy Environ. Sci.* **2013**, *6*, 148–156.

(21) Kuhn, A.; Gerbig, O.; Zhu, C.; Falkenberg, F.; Maier, J.; Lotsch, B. V. A New Ultrafast Superionic Li-Conductor: Ion Dynamics in $Li_{11}Si_2PS_{12}$ and Comparison with Other Tetragonal LGPS-type Electrolytes. *Phys. Chem. Chem. Phys.* **2014**, *16*, 14669–14674.

(22) Adeli, P.; Bazak, J. D.; Park, K. H.; Kochetkov, I.; Huq, A.; Goward, G. R.; Nazar, L. F. Boosting Solid-State Diffusivity and Conductivity in Lithium Superionic Argyrodites by Halide Substitution. *Angew. Chemie Int. Edn.* **2019**, *58*, 8681–8686.

(23) De Klerk, N. J.; Rosłoń, I.; Wagemaker, M. Diffusion Mechanism of Li Argyrodite Solid Electrolytes for Li-Ion Batteries and Prediction of Optimized Halogen Doping: The Effect of Li Vacancies, Halogens, and Halogen Disorder. *Chem. Mater.* **2016**, *28*, 7955–7963.

(24) Minafra, N.; Kraft, M. A.; Bernges, T.; Li, C.; Schlem, R.; Morgan, B. J.; Zeier, W. G. Local Charge Inhomogeneity and Lithium Distribution in the Superionic Argyrodites $Li_6PS_5X$ (X = Cl, Br, I). *Inorg. Chem.* **2020**, *59*, 11009–11019.

(25) Yu, C.; Ganapathy, S.; Hageman, J.; Van Eijck, L.; Van Eck, E. R.; Zhang, L.; Schwietert, T.; Basak, S.; Kelder, E. M.; Wagemaker, M. Facile Synthesis toward the Op-

timal Structure-Conductivity Characteristics of the Argyrodite $Li_6PS_5Cl$ Solid-State Electrolyte. *ACS Appl. Mater. Interfaces* **2018**, *10*, 33296–33306.

(26) Harm, S.; Hatz, A. K.; Moudrakovski, I.; Eger, R.; Kuhn, A.; Hoch, C.; Lotsch, B. V. Lesson Learned from NMR: Characterization and Ionic Conductivity of LGPS-like $Li_7SiPS_8$. *Chem. Mater.* **2019**, *31*, 1280–1288.

(27) Kudu, Ö. U.; Famprikis, T.; Fleutot, B.; Braida, M. D.; Le Mercier, T.; Islam, M. S.; Masquelier, C. A Review of Structural Properties and Synthesis Methods of Solid Electrolyte Materials in the $Li_2S-P_2S_5$ Binary System. *J. Power Sources* **2018**, *407*, 31–43.

(28) Mizuno, F.; Hayashi, A.; Tadanaga, K.; Tatsumisago, M. New, Highly Ion-Conductive Crystals Precipitated from $Li_2S$-$P_2S_5$ Glasses. *Adv. Mater.* **2005**, *17*, 918–921.

(29) Minami, K.; Hayashi, A.; Tatsumisago, M. Preparation and Characterization of Superionic Conducting $Li_7P_3S_{11}$ Crystal from Glassy Liquids. *J. Ceram. Soc. Japan* **2010**, *118*, 305–308.

(30) Hayashi, A.; Minami, K.; Tatsumisago, M. Development of Sulfide Glass-Ceramic Electrolytes for All-Solid-State Lithium Rechargeable Batteries. *J. Solid State Electrochem.* **2010**, *14*, 1761–1767.

(31) Hayashi, A.; Shigenori, H.; Morimoto, H.; Tatsumisago, M.; Minami, T. Preparation of $Li_2S$-$P_2S_5$ Amorphous Solid Electrolytes by Mechanical Milling. *J. Am. Ceram. Soc.* **2001**, *84*, 477–479.

(32) Xue, B.; Fan, B.; Li, B.; Chen, L.; Wang, F.; Luo, Z.; Zhang, X.; Ma, H. Solvent-Assisted Ball Milling for Synthesizing Solid Electrolyte $Li_7P_3S_{11}$. *Journal of the American Ceramic Society* **2019**, *102*, 3402–3410.

(33) Zhao, F.; Alahakoon, S. H.; Adair, K.; Zhang, S.; Xia, W.; Li, W.; Yu, C.; Feng, R.; Hu, Y.; Liang, J., et al. An Air-Stable and Li-Metal-Compatible Glass-Ceramic Electrolyte enabling High-Performance All-Solid-State Li Metal Batteries. *Advanced Materials* **2021**, *33*, 2006577.

(34) Preefer, M. B.; Grebenkemper, J. H.; Schroeder, F.; Bocarsly, J. D.; Pilar, K.; Cooley, J. A.; Zhang, W.; Hu, J.; Misra, S.; Seeler, F.; Schierle-Arndt, K.; Seshadri, R. Rapid and Tunable Assisted-Microwave Preparation of Glass and Glass-Ceramic Thiophosphate "$Li_7P_3S_{11}$" Li-Ion Conductors. *ACS Appl. Mater. Interfaces* **2019**, *11*, 42280–42287.

(35) Suto, K.; Bonnick, P.; Nagai, E.; Niitani, K.; Arthur, T. S.; Muldoon, J. Microwave-Aided Synthesis of Lithium Thiophosphate Solid Electrolyte. *J. Mater. Chem A* **2018**, *6*, 21261–21265.

(36) Ito, S.; Nakakita, M.; Aihara, Y.; Uehara, T.; Machida, N. A Synthesis of Crystalline $Li_7P_3S_{11}$ Solid Electrolyte from 1, 2-dimethoxyethane Solvent. *J. Power Sources* **2014**, *271*, 342–345.

(37) Wang, Y.; Lu, D.; Bowden, M.; Khoury, P. Z. E.; Han, K. S.; Deng, Z. D.; Xiao, J.; Zhang, J.-g.; Liu, J. Mechanism of Formation of $Li_7P_3S_{11}$ Solid Electrolytes through Liquid Phase Synthesis. *Chem. Mater.* **2018**, *30*, 990–997.

(38) Ghidiu, M.; Ruhl, J.; Culver, S. P.; Zeier, W. G. Solution-Based Synthesis of Lithium Thiophosphate Superionic Conductors for Solid-State Batteries: A Chemistry Perspective. *J. Mater. Chem A* **2019**, *7*, 17735–17753.

(39) Busche, M. R.; Weber, D. A.; Schneider, Y.; Dietrich, C.; Wenzel, S.; Leichtweiss, T.; Schröder, D.; Zhang, W.; Weigand, H.; Walter, D.; Sedlmaier, S. J.; Houtarde, D.; Nazar, L. F.; Janek, J. In Situ Monitoring of Fast Li-Ion Conductor $Li_7P_3S_{11}$ Crystallization Inside a Hot-Press Setup. *Chem. Mater.* **2016**, *28*, 6152–6165.

(40) Garcia-Mendez, R.; Smith, J. G.; Neuefeind, J. C.; Siegel, D. J.; Sakamoto, J. Correlating Macro and Atomic Structure with Elastic Properties and Ionic Transport of Glassy $Li_2S-P_2S_5$ (LPS) Solid Electrolyte for Solid-State Li Metal Batteries. *Adv. Energy Mater.* **2020**, *10*, 2000335.

(41) Ohno, S. et al. How Certain Are the Reported Ionic Conductivities of Thiophosphate-Based Solid Electrolytes? An Interlaboratory Study. *ACS Energy Lett.* **2020**, *5*, 910–915.

(42) Mizuno, F.; Hayashi, A.; Tadanaga, K.; Tatsumisago, M. New Lithium-Ion Conducting Crystal Obtained by Crystallization of the $Li_2S$-$P_2S_5$ glasses. *Electrochem. Solid-State Lett.* **2005**, *8*, 603–606.

(43) Toby, B. H.; Von Dreele, R. B. GSAS-II: The Genesis of a Modern Open-Source All Purpose Crystallography Software Package. *J. Appl. Crystallogr.* **2013**, *46*, 544–549.

(44) Juhás, P.; Davis, T.; Farrow, C. L.; Billinge, S. J. PDFgetX3: A Rapid and Highly Automatable Program for Processing Powder Diffraction Data into Total Scattering Pair Distribution Functions. *J. Appl. Crystallogr.* **2013**, *46*, 560–566.

(45) Farrow, C.; Juhas, P.; Liu, J.; Bryndin, D.; Božin, E.; Bloch, J.; Proffen, T.; Billinge, S. PDFfit2 and PDFgui: Computer Programs for Studying Nanostructure in Crystals. *J. Phys. Condens. Matter* **2007**, *19*, 335219.

(46) Meyer, W.; Neldel, H. Relation Between the Energy Constant and the Quantity Constant in the Conductivity–Temperature Formula of Oxide Semiconductors. *Z. Tech. Phys* **1937**, *18*, 588–593.

(47) Mizuno, F.; Hayashi, A.; Tadanaga, K.; Tatsumisago, M. High Lithium Ion Conducting Glass-Ceramics in the System $Li_2S$-$P_2S_5$. *Solid State Ionics* **2006**, *177*, 2721–2725.

(48) Tilley, R. J. *Defects in Solids*; John Wiley & Sons, 2008.

(49) Yelon, A.; Movaghar, B. The Meyer-Neldel Conductivity Prefactor for Chalcogenide Glasses. *Appl. Phys. Lett.* **1997**, *71*, 3549–3551.

(50) Dietrich, C.; Weber, D. A.; Sedlmaier, S. J.; Indris, S.; Culver, S. P.; Walter, D.; Janek, J.; Zeier, W. G. Lithium Ion Conductivity in $Li_2S$–$P_2S_5$ Glasses-Building Units and Local Structure Evolution during the Crystallization of Superionic Conductors $Li_3PS_4$, $Li_7P_3S_{11}$ and $Li_4P_2S_7$. *J. Mater. Chem. A* **2017**, *5*, 18111–18119.

(51) Minami, K.; Mizuno, F.; Hayashi, A.; Tatsumisago, M. Lithium Ion Conductivity of the $Li_2S$-$P_2S_5$ Glass-Based Electrolytes Prepared by the Melt Quenching Method. *Solid State Ionics* **2007**, *178*, 837–841.

(52) Minami, K.; Hayashi, A.; Tatsumisago, M. Crystallization Process for Superionic $Li_7P_3S_{11}$ Glass-Ceramic Electrolytes. *J. Am. Ceram. Soc.* **2011**, *94*, 1779–1783.

# Graphical TOC entry

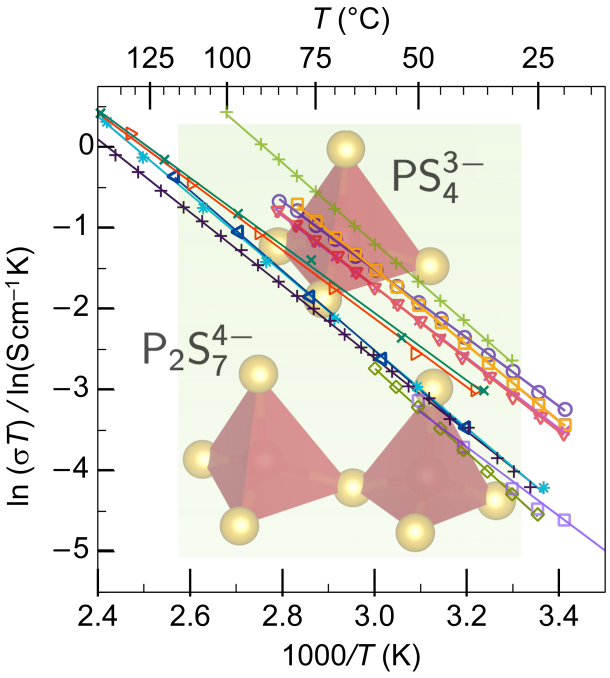

# Supporting Information:

# Subtle Local Structural Details Influence Ion Transport in Glassy $Li^+$ Thiophosphate Solid Electrolytes

Molleigh B. Preefer,[*,†,‡] Jason H. Grebenkemper,[‡] Catrina E. Wilson,[†] Margaux Everingham,[†] Joya A. Cooley,[¶] and Ram Seshadri[*,‡,†]

†*Department of Chemistry and Biochemistry*

*University of California, Santa Barbara, California 93106, United States*

‡*Materials Department and Materials Research Laboratory*

*University of California, Santa Barbara, California 93106, United States*

¶*Department of Chemistry and Biochemistry*

*California State University, Fullerton, California 92834, United States*

E-mail: mpreefer@mrl.ucsb.edu; seshadri@mrl.ucsb.edu

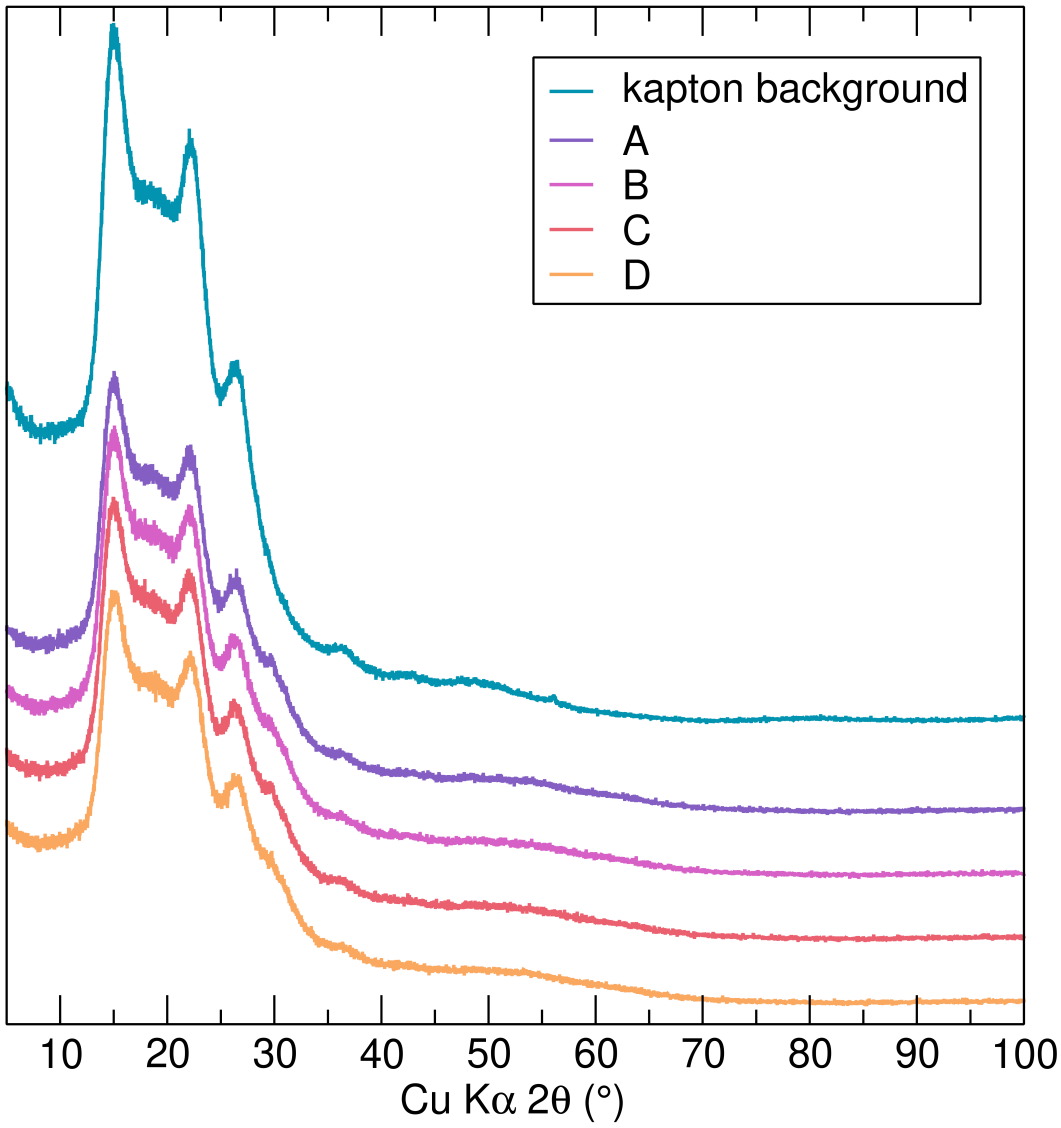


Figure S.1: Laboratory X-ray diffraction patterns of the four samples af the glassy $Li^+$ thiophosphates **A** through **D** described in this work. The kapton background included shows the pattern obtained from the air-free sample holder. The samples do not add any crystalline peaks to the amorphous background.

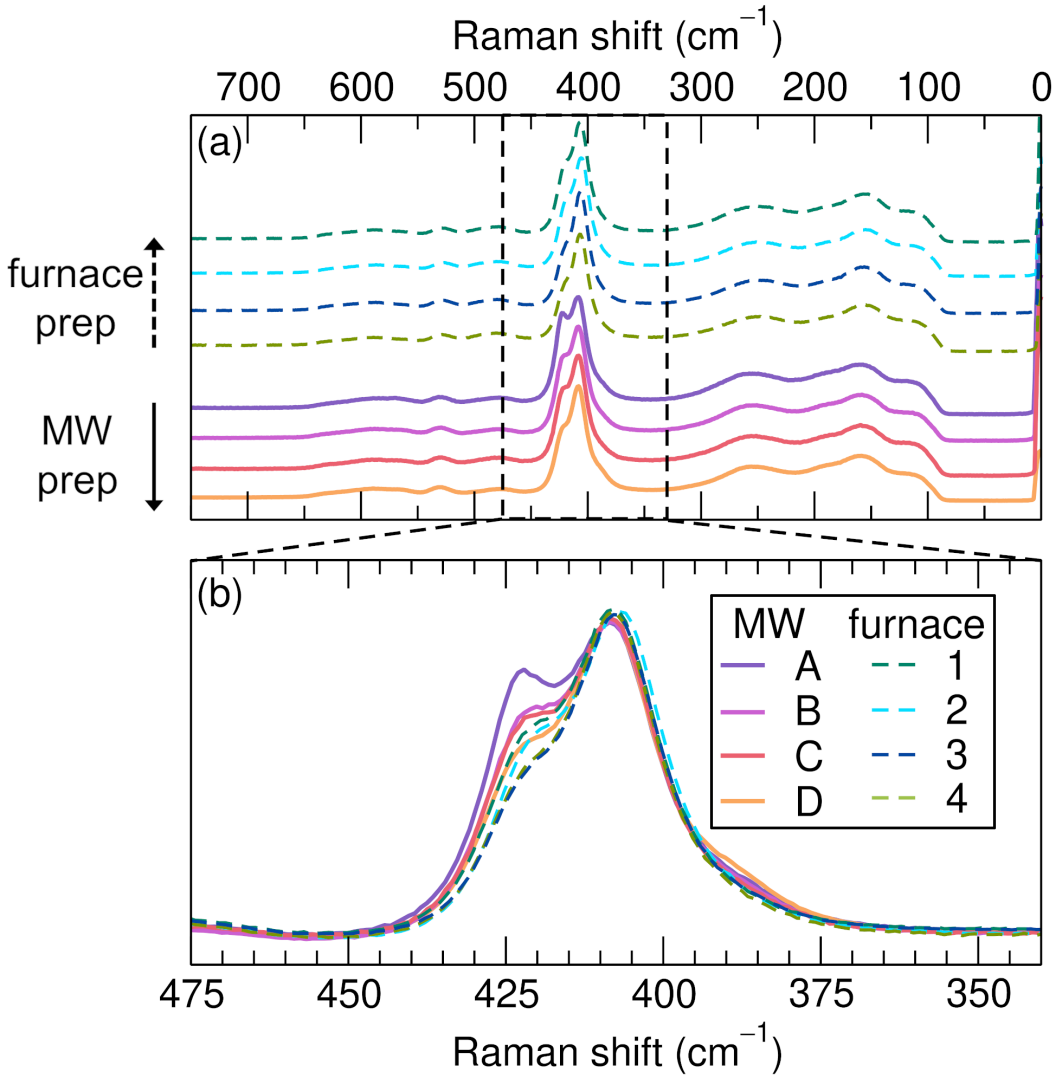


Figure S.2: A comparison of the key regions of the Raman spectra of glassy $Li^+$ thiophosphates prepared using microwave heating (described throughout the main text, solid lines) with a set of samples prepared more conventionally through furnace heating (dashed lines), showing the same local structure variability arises irrespective of preparation. For both sets of samples, 4 samples were prepared using either the microwave heating method (samples **A** through **D**) or furnace heating method (samples **1** through **4**). Both methods are explained in the methods section in the main text. (a) The full spectral range acquired from 0 cm$^{-1}$ to 750 cm$^{-1}$ is shown. For clarity (b) shows a narrower range from 340 cm$^{-1}$ to 475 cm$^{-1}$ to better compare the variations in relative ratios of corner-sharing tetrahedra to isolated tetrahedra in the local structure.

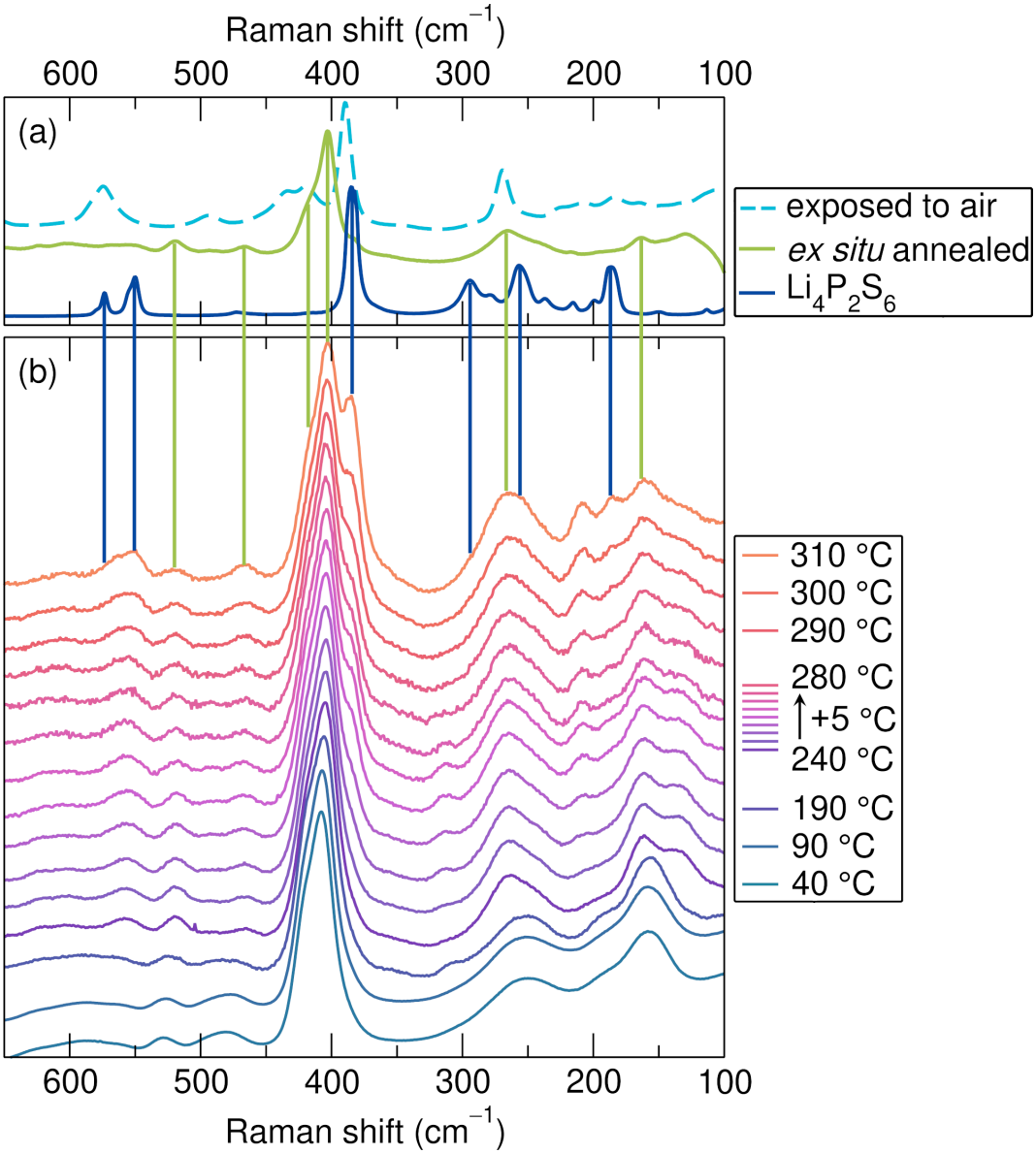


Figure S.3: Thermal evolution of the Raman spectra of a glass (sample **D**), showing the complete Raman shift range acquired, with the data offset for clarity. (a) The control experiments are shown, including a sample that was purposefully exposed to air, which is plotted in a light blue dashed line. We believe there is no evidence for air exposure throughout the experiment, as the modes do not align with what is observed during the *in situ* experiment. The modes that evolve with annealing match the position of the modes observed in an *ex situ* annealed glass sample (which crystallizes into $Li_7P_3S_{11}$) shown in green, and $Li_4P_2S_6$, which is the thermodynamically-stable crystalline phase that often emerges, shown in dark blue. The lines drawn are to guide the eye to the existing modes in the *in situ* temperature series, (b).

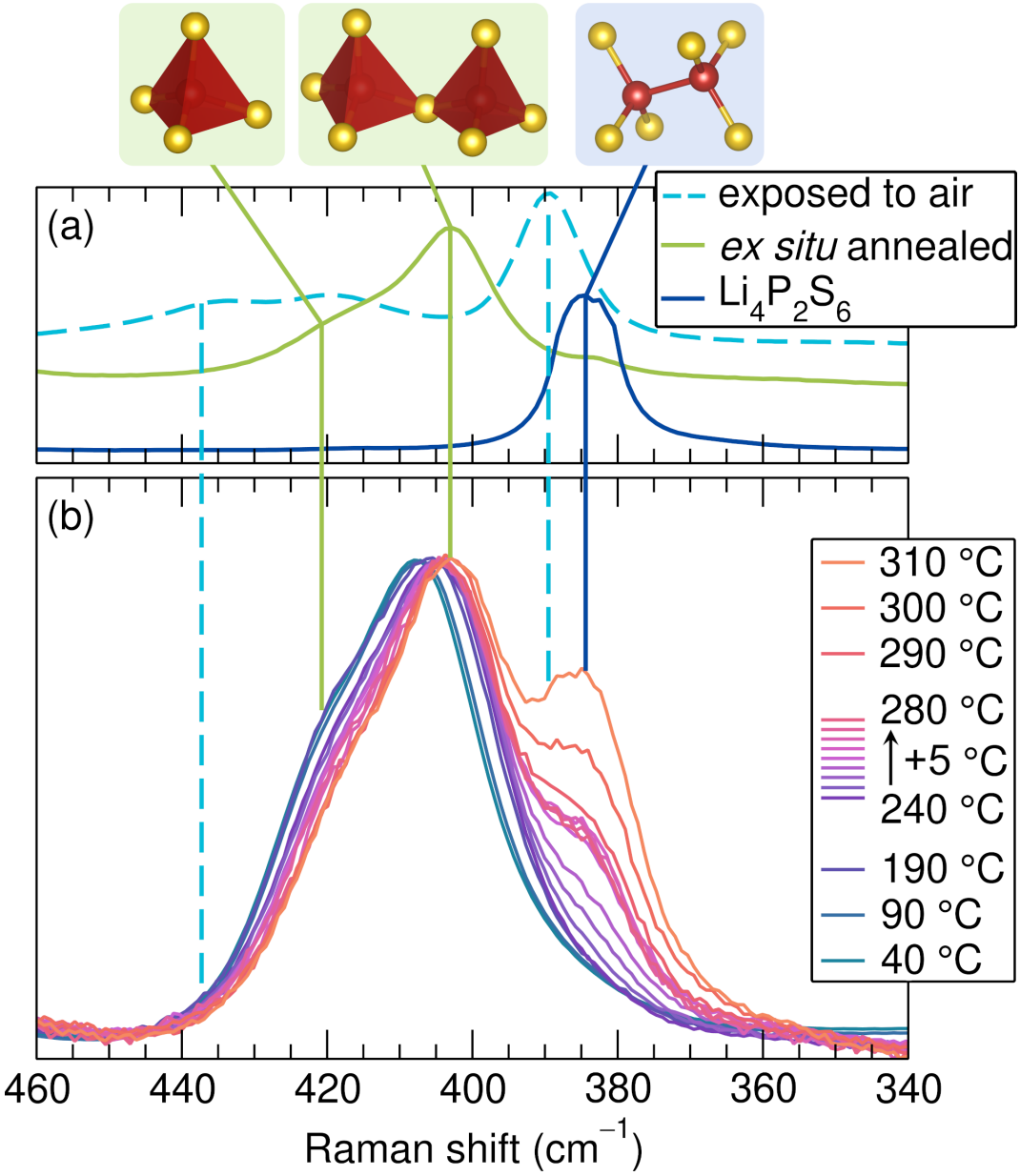


Figure S.4: Thermal evolution of the Raman spectra of a glass (sample **D**), in the same narrower range as shown in the main text, with overlapping spectra in order to compare the relative ratios of the different representative modes present. (a) The control experiments are shown, including a sample that was purposefully exposed to air, which is plotted in a light blue dashed line. We believe there is no evidence for air exposure throughout the experiment, as the modes do not align with what is observed during the *in situ* experiment. The modes that evolve with annealing match the position of the modes observed in an *ex situ* annealed glass sample (which crystallizes into $Li_7P_3S_{11}$) shown in green, and $Li_4P_2S_6$, which is the thermodynamically-stable crystalline phase that often emerges, shown in dark blue. The lines drawn are to guide the eye to the existing modes in the *in situ* temperature series, (b).